

IN THE SPECIFICATION

Please amend the specification to add brief descriptions to the Figures and to correct minor typographical errors in the specification due to the removal of the Figures from the body of the text. The Applicant's undersigned attorney respectfully asserts that no new matter has been introduced by these amendments.

In the Brief Description of Drawings

Please insert the following new paragraphs after the description for Figure 1.

Figure 2 is a graph of the vibration sensitivity of a particular spindle to maximum capacity balance correction.

Figure 3.1 is a graph of a single active balancing control stable for all values of the gain multiplied by the quotient of the actual and estimated influence coefficients which are falling with the unit circle in the right half complex plane.

Figure 3.2 is a graph of the forgetting factor with a normalized variance of influence coefficient estimate.

Figure 3.3 is a graph of the number of estimation iterations required for 95% convergence of the estimate for varying forgetting factor values.

Figure 3.4 is a schematic block diagram of an adaptive influence coefficient control system.

Figure 3.5 is a flow chart of experimental single plane active balancing control system.

Figure 3.6 is a graph of the vibration sensitivity phase angle of the particular spindle shown in Figure 2.

Figure 3.7 is a graph of the measure spindle housing vibration during active balancing of a nonlinear system.

Figure 3.8 is a graph of the measured time-frequency spectrum of spindle housing vibration showing broadband effect of active balancing of nonlinear systems.

Figure 3.9 is a graph of measured spindle housing vibration during single-plane adaptive active balancing with an inaccurate initial influence coefficient estimate.

Figure 3.10 is a graph of measured spindle housing vibration during single-plane active balancing after adaptive system “learning”.

Figure 3.11 is a graph of measured spindle vibration before and after adaptive active balancing at various spindle speeds.

Figure 3.12 is a graph of the normalized magnitude and phase of balance correction required to minimize vibration at each spindle speed.

Figure 4.1 is a graph of simulated adaptive control response and infinite argument magnitude of equation 4.2.

Figure 4.2 is a graph of the automatically tuned parameter values as functions of influence coefficient estimation error.

Figure 4.3 is graph of the hysteresis band between the supervisory limits which reduce spurious control activation.

Figure 4.4 is a graph of the experimental results using automatic supervisory control limit setting with auto-tuning active balance system.

Figure 4.5 is a pair of graphs of spindle housing vibration during active balancing using conventional fixed parameter adaptive control and auto-tuning adaptive control with erroneous initial influence coefficient estimates.

Figure 4.6 is a collection of graphs comparing active balancing control performance of auto-tuning control and conventional fixed parameter adaptive control with erroneous initial influence estimates.

Figure 4.7 is a pair of graphs depicting spindle housing vibration during active balancing using cautious conventional fixed-parameter adaptive control and auto-tuning adaptive control with erroneous initial influence coefficient estimates.

Figure 4.8 is a collection of graphs comparing active balancing control performance using cautious conventional fixed-parameter adaptive control auto-tuning with erroneous initial influence estimates.

Figure 4.9 is a pair of graphs depicting spindle housing vibration during active balancing using conventional adaptive control and auto-tuning adaptive control with accurate initial influence coefficient estimates.

Figure 4.10 is a collection of graphs comparing active balancing control performance of conventional fixed-parameter adaptive and control auto-tuning control with accurate initial influence coefficient estimates.

Figure 5.1 is a flow chart of supervisory adaptive optimal control for multiple-plane active balancing systems.

Figure 5.2 is a table of the average measured balancing influence matrix at 3,100 RPM.

Figure 5.3 is a graph of the predicted mode shapes of a flexible rotor test rig for two critical speeds.

Figure 5.4 is a graph of the predicted force response deflected shape of a rotor at 3,100 RPM due to 0.34 Oz-In. unbalance at drive-end active balancing plane.

Figure 5.5 is a pair of graphs comparing adaptive optimal control results using single-plane and dual plane active balancing.

Figure 5.6 is a pair of graphs comparing the results of adaptive optimal control with and without control effort penalty.

Figure 5.7 is a pair of graphs depicting the results of fully output dithered adaptive optimal control of a lightly cross-coupled system.

Figure 5.8 is a collection of graphs depicting the dual-plane optimal active balancing control results for a somewhat inaccurate initial influence matrix estimate.

Figure 5.9 is a pair of graphs depicting the objective function response and estimated stability criterion during optimal active balancing control with an erroneous initial influence matrix estimate.

Figure 5.10 is a collection of graphs depicting the results of non-adaptive and adaptive optimal control strategies.

IN THE SPECIFICATION

In the specification at page 11, lines 5-11 (clean version)

This criterion can be represented graphically in the complex plane as shown in Figure 3.1.

From Figure 3.1, one can see how the control gain parameter α can enhance robustness. For the case in which the actual influence coefficient does not change during control convergence, it can be shown, based on Eq. (3.11), that the non-adaptive control law of Eq. (3.3) is stable if and only if

$$\alpha < 2 \frac{|\hat{c}|}{|c|} \cos(\theta_c - \theta_{\hat{c}}) \quad \text{Eq. (3.12)}$$

In the specification at page 14, lines 1 - 3 (clean version)

Thus, the estimation variance can be reduced by selecting a low value for β . For values of β close to unity, the estimation variance approaches the variance of the calculated parameter c_{new} . This relationship is shown in Figure 3.2.

In the specification at page 14, lines 10 - 13 (clean version)

where c is the actual influence coefficient, \hat{c}_0 is the initial estimate and $E[\hat{c}_k]$ is the expected value of the influence coefficient estimate after k iterations. The number of estimation iteration required for 95% convergence of the estimate for varying β values is plotted in Figure 3.3.

In the specification at page 14, lines 19 – 21 and page 15, line 1 - 2 (clean version)

With the addition of the control gain α and the on-line influence coefficient estimation, the adaptive single plane recursive control law is given by

$$w_{k+1} = w_k - \alpha \left(\frac{e_k}{\hat{c}_k} \right) \quad \text{Eq. (3.17)}$$

where \hat{c}_k is given in Eq. (3.14). The block diagram form of the controller is shown in Figure 3.4.

In the specification at page 21, lines 12 - 21 (clean version)

A significantly useful side benefit of the active balancing system is that it can be used as a probe to measure and track the unbalance response of a system. Such system

identification information contains useful data about the dynamic bearing stiffness and effective rotating mass. For the experiment discussed above, the unbalance sensitivity was stored at each speed every time the active balancing system was enabled to control vibration. This data was obtained for two spindle system configurations to allow for comparisons. A long tool and short tool were separately inserted into the spindle and active balancing control enabled for successive rotational speeds. Figure 2 and Figure 3.6 show the measured unbalance sensitivity amplitude and phase angle for the two tool configurations.

In the specification at page 33, lines 21 - 23 (clean version)

The automatic supervisory limit selection method was enabled during the experimental testing. Figure 4.4 shows the automatically calculated supervisory limit settings from the experiment shown in Figure 4.6.

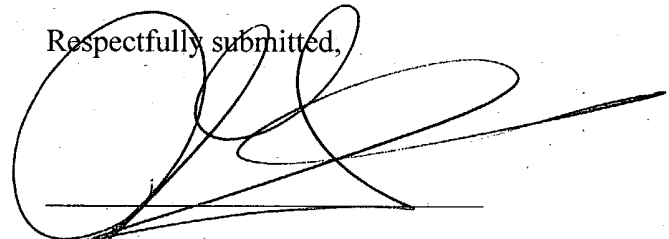
In the specification at page 47, lines 13 – 23 and page 48, lines 1 - 4 (clean version)

To test the active balancing system for a plant with fairly “rich” rotordynamics the rotor was run at about 3,100 rpm during the experiments. Since this speed was in between the first two critical speeds, both mode shapes contributed significantly to dynamic response. Figure 5.4 shows the predicted forced-response deflected shape of the rotor due to a 0.34 oz-in unbalance at the drive-end (left end) active balancing plane. This unbalance represented the maximum correction capacity of the active balancing device. Figure 5.4 could be used to predict the influence coefficient at 3,100rpm from the drive-end active balancing device to the two sensors. The combination of contributions of the two mode shapes at 3,100 rpm provides for a relatively interesting response situation. Note that unbalance at the drive end balance has

a much greater influence on shaft response at the outboard sensor than on the drive-end sensor. Since the rotor configuration is highly symmetrical, the outboard balance plane also has the greatest influence on the drive-end sensor. The actual experimental results matched this prediction fairly well in a qualitative sense. The average measured influence matrix between both balance planes and four sensors at 3,100 rpm is presented in the table shown in Figure 5.2.

The above amendments to the specification reflect the removal of the drawings from the body of the specification in the parent application 09/282,755 and have been made to reflect the removal and renumbering of some of the Figures. If the Examiner has any questions regarding this matter, the Examiner is invited to call Applicant's undersigned attorney at (248) 324-7787.

Respectfully submitted,

A handwritten signature in black ink, consisting of a large, stylized 'J' followed by a series of loops and a long horizontal stroke extending to the right.

John G. Chupa (Reg. No. 33,483)
Law Offices of John Chupa & Associates
28535 Orchard Lake Rd., Suite 50
Farmington Hills, MI 48334
Attorney for Applicants

MARKED UP VERSION OF AMENDED SPECIFICATION PARAGRAPHS

Please amend the specification at page 11, lines 5 - 11 as follows:

This criterion can be represented graphically in the complex plane as shown in Figure [3.2] 3.1.

From Figure [3.2] 3.1, one can see how the control gain parameter α can enhance robustness. For the case in which the actual influence coefficient does not change during control convergence, it can be shown, based on Eq. (3.11), that the non-adaptive control law of Eq. (3.3) is stable if and only if

$$\alpha < 2 \frac{|\hat{c}|}{|c|} \cos(\theta_c - \theta_{\hat{c}}) \quad \text{Eq. (3.12)}$$

Please amend the specification at page 14, lines 1 - 3 as follows:

Thus, the estimation variance can be reduced by selecting a low value for β . For values of β close to unity, the estimation variance approaches the variance of the calculated parameter c_{new} . This relationship is shown in Figure [3.3a] 3.2.

Please amend the specification at page 14, lines 10 - 13 as follows:

where c is the actual influence coefficient, \hat{c}_0 is the initial estimate and $E[\hat{c}_k]$ is the expected value of the influence coefficient estimate after k iterations. The number of estimation iteration required for 95% convergence of the estimate for varying β values is plotted in Figure [3.3b] 3.3.

Please amend the specification at page 14, lines 19 – 21 and page 15, line 1 - 2 as follows:

With the addition of the control gain α and the on-line influence coefficient estimation, the adaptive single plane recursive control law is given by

$$w_{k+1} = w_k - \alpha \left(\frac{e_k}{\hat{c}_k} \right) \quad \text{Eq. (3.17)}$$

where \hat{c}_k is given in Eq. (3.14). The block diagram form of the controller is shown in [the] Figure [below] 3.4.

Please amend the specification at page 21, lines 12 - 21 as follows:

A significantly useful side benefit of the active balancing system is that it can be used as a probe to measure and track the unbalance response of a system. Such system identification information contains useful data about the dynamic bearing stiffness and effective rotating mass. For the experiment discussed above, the unbalance sensitivity was stored at each speed every time the active balancing system was enabled to control vibration. This data was obtained for two spindle system configurations to allow for comparisons. A long tool and short tool were separately inserted into the spindle and active balancing control enabled for successive rotational speeds. Figure [3.13] 2 and Figure [3.14 below] 3.6 show the measured unbalance sensitivity amplitude and phase angle for the two tool configurations.

Please amend the specification at page 33, lines 21 - 23 as follows:

The automatic supervisory limit selection method was enabled during the experimental testing. Figure [4.11] 4.4 shows the automatically calculated supervisory limit settings from the experiment shown in Figure 4.6.

Please amend the specification at page 47, lines 13 – 23 and page 48, lines 1 - 4 as follows:

To test the active balancing system for a plant with fairly “rich” rotordynamics the rotor was run at about 3,100 rpm during the experiments. Since this speed was in between the first two critical speeds, both mode shapes contributed significantly to dynamic response. Figure 5.4 shows the predicted forced-response deflected shape of the rotor due to a 0.34 oz-in unbalance at the drive-end (left end) active balancing plane. This unbalance represented the maximum correction capacity of the active balancing device. Figure 5.4 could be used to predict the influence coefficient at 3,100rpm from the drive-end active balancing device to the two sensors. The combination of contributions of the two mode shapes at 3,100 rpm provides for a relatively interesting response situation. Note that unbalance at the drive end balance has a much greater influence on shaft response at the outboard sensor than on the drive-end sensor. Since the rotor configuration is highly symmetrical, the outboard balance plane also has the greatest influence on the drive-end sensor. The actual experimental results matched this prediction fairly well in a qualitative sense. The average measured influence matrix between both balance planes and four sensors at 3,100 rpm is presented in the table shown in Figure 5.2 [Table 5.1].